Hierarchically Porous Iron Alloys with High Sintering Resistance During Cyclic Steam Oxidation and Hydrogen Reduction

Author(s):
Pennell, Samuel M.; Chappuis, Benoît; Carpenter, Julia A.; Dunand, David C.

Publication date:
2023-12-08

Permanent link:
https://doi.org/10.3929/ethz-b-000631826

Originally published in:
Advanced Functional Materials 33(50), https://doi.org/10.1002/adfm.202307470

ADVANCED FUNCTIONAL MATERIALS
www.afm-journal.de

Hierarchically Porous Iron Alloys with High Sintering Resistance During Cyclic Steam Oxidation and Hydrogen Reduction

Samuel M. Pennell, Benoît Chappuis, Julia A. Carpenter, and David C. Dunand*

Hydrogen release/storage materials for iron/air batteries are fabricated as Fe-16Mo and Fe-24Ni (at.%) lattices via 3D-extrusion printing of foamed inks containing oxide microparticles, followed by H_2 reduction and sintering. A hierarchical open porosity is designed: (i) channels between walls created during printing, (ii) mesopores within walls, created during ink foaming, and (iii) micropores within ligaments between mesopores, created from partial sintering metal particles and gas escape during cycling. When subjected to H_2/H_2O redox cycling at 800 °C, the lattices of both compositions gradually undergo sintering. The Fe-16Mo lattice remains fully redox-active after 50 cycles unlike the Fe-24Ni lattice, which loses 90% of its redox capacity after 30 cycles. The increased lifetime of the Fe-16Mo lattice is attributed to the sintering inhibition of Mo, the formation of a mixture of oxide phases in the oxidized state, and the cyclic formation of submicron Fe_2Mo by reduction of MoO_2 and $Fe_2Mo_3O_8$. The microstructure of the foamed walls is examined throughout cycling to track changes in morphology and composition. These are correlated to volume and porosity changes in the lattice. A comparison is made to previously-studied Fe-Mo and Fe-Ni freeze-cast lamellar foams, and variations in performance are discussed in the context of the different architectures.

1. Introduction

Redox-active Fe-based materials have promising characteristics for low-cost redox cycling, either for electrical energy storage when paired with a reversible solid oxide fuel cell (RSOFC) to form a rechargeable oxide battery (ROB) [1–5] or for chemical looping combustion.[6–8] During the first part of the redox cycle, iron is oxidized by steam ($3Fe + 4H_2O \rightarrow Fe_3O_4 + 4H_2$), and the produced hydrogen can be used to fuel the RSOFC using oxygen from air to form steam and electric power. During subsequent reduction, hydrogen (produced via steam electrolysis in the RSOFC) reduces the oxide back to iron: $Fe_3O_4 + 4H_2 \rightarrow 3Fe + 4H_2O$). The basic configuration of the ROB is depicted schematically in Figure S1, Supporting Information, a chamber containing the redox material (i.e., Fe) and H_2O is sealed by the RSOFC. Developments to the ROB design can improve performance by separating the redox material from the fuel cell or inducing gas flow rather than letting the gas stagnate,[9,10] but the redox reactions remain the same. This iron-air battery uses inexpensive, abundant, and environmentally-benign materials: iron oxide, water, and oxygen from air.

However, the development of high-temperature redox systems using Fe-based powder beds has been significantly hindered by the degradation of Fe-based materials during repeated redox cycling.[4,5,7,11] The volumetric expansion of iron during oxidation ($3Fe \rightarrow Fe_3O_4$) combined with the high operating temperature of the RSOFC lead to irreversible sintering between particles. This sintering process quickly leads to densification of the initially porous material, greatly slowing the kinetics of the reaction as incoming gas can no longer flow through the pores of the material. For a Fe powder-packed bed, H_2 production drops by 66% after just two cycles and continues dropping towards a negligible amount of H_2 produced after ten cycles.[12]

Two approaches can be used to improve performance without altering the operating temperature or gas flow conditions: compositional changes (at the level of the material itself) and alternate architectures (at the level of the spatial structure of the specimen). By either alloying the Fe with other metals or by including other

S. M. Pennell, D. C. Dunand
Department of Materials Science and Engineering
Northwestern University
Evanston, IL 60208, USA
E-mail: samuelpennell2024@u.northwestern.edu
B. Chappuis
ETH Zürich
Complex Materials
8093 Zürich, Switzerland
B. Chappuis, J. A. Carpenter
Apheros AG
8093 Zürich, Switzerland

The ORCID identification number(s) for the author(s) of this article can be found under https://doi.org/10.1002/adfm.202307470

DOI: 10.1002/adfm.202307470

oxides in the Fe powder mixture, the properties of the overall material during cycling can be altered. Otsuka et al. completed a survey of 26 individual elemental additives to iron, assessing their impact on H_2 production in the first five redox cycles; this study, identified elements with stable oxide states under steam (such as Al and Ce) as stabilizing for the Fe powder bed, and elements that do not oxidize (such as Ni and Cu) as destabilizing.[13] The effect of redox inactive elements remains unclear however: Eigen et al. reported beneficial effects of Ni additions in Fe powder bed systems, up to 104 cycles,[14] Yüzbasi et al. reported a beneficial effect of Cu on accelerating Fe_3O_4 reduction in chemical looping systems,[15] and Ma et al. reported beneficial effect of yttria stabilized zirconia (YSZ) on H_2 production from Fe.[16]

In particular, Mo was identified as having a strong beneficial effect on the reaction kinetics and stability of Fe-Mo alloyed powders, an effect confirmed in similar experiments.[17] Mo, along with W, are two elements that are redox active under both steam and hydrogen; this makes them candidates for pure Mo or pure W rechargeable oxide batteries, as the oxides formed (MoO_2 and WO_2) have a higher oxygen-to-metal atomic ratio than Fe_3O_4.[18,19]

The reaction mechanisms of both oxidation and reduction are vital to understand the microstructural evolution of materials undergoing redox cycling. For both binary Fe and Mo oxides, and for the mixed oxides formed from Fe-Mo alloys as well, oxidation with steam proceeds through a multi-step process: first, the steam adsorbs on the metal surface, then the steam reacts with the metal to form the oxide (as the H_2O dissociates), then the newly formed H_2 desorbs.[20,21] After the initial surface oxide layer forms, the reaction rate is controlled by the diffusion of metal atoms to the surface and the counter-diffusion of oxygen anions into the bulk, with the reaction occurring in the bulk oxide layer.[20,21] As oxidation proceeds and the oxide scale grows in thickness (and as FeO is oxidized to Fe_3O_4), the reaction slows due to the increasing diffusion distance and the slower diffusion of atoms through the outer scale as compared to the metal.[22]

While Mo oxidizes via the same mechanism as Fe, steam oxidation of Mo introduces an additional variable. MoO_2 forms a high-vapor pressure phase ($MoO_2(OH)_2$) with steam at high temperature, resulting in the gradual loss of Mo from the surface due to chemical vapor transport (CVT).[23,24]

Reduction of iron oxides (Fe_3O_4 and FeO) typically proceeds following the shrinking core model, wherein the oxides at the outer surface reduce first, forming a characteristic dense metal shell through which subsequent H_2 must either diffuse or otherwise bypass in order to reduce the underlying oxide.[25] The reduction reaction is known to be accelerated by the presence of transition metals (including Ni), such that the reduction reaction begins at the interface between the oxide and the transition metal and proceed along the moving interface (i.e., inside out).[26–28]

High-temperature H_2 reduction of MoO_2 (and $Fe_2Mo_3O_8$) proceeds via a different mechanism. As mentioned above, the gaseous $MoO_2(OH)_2$ forms at high temperatures in the presence of steam. This mechanism is also active during reduction, wherein H_2 reduces gaseous $MoO_2(OH)_2$ to Mo, resulting in Mo condensation at the operating temperature.[29] This CVT reduction mechanism strongly influences the morphology of the precipitated Mo phase, resulting in a spherical nanocrystalline morphology.[30] In the presence of Fe, this nanocrystalline Mo phase quickly reacts with Fe to form nanocrystalline Fe_2Mo.[31,32]

Both oxidation and reduction are enhanced by high porosity. During oxidation, high porosity shortens the diffusion distance between unreacted metal atoms and the nearest free surface, lowering the transport time needed. During reduction, high porosity allows the surface-driven reduction reaction to begin throughout the material rather than solely at the envelope-free surface, and pores locally prevent the formation of a dense shell that could slow gas ingress.

Our previous work also sought to address the degradation problem by altering the architecture of the Fe-based material away from a packed powder bed. In particular, we examined directional freeze-casting to produce lamellar Fe architectures compatible with flow reactions. These lamellar Fe structures, with high porosity and low tortuosity ideal for solid-gas reactions,[33] were shown to extend the useful redox lifetime of the Fe-based material, particularly with alloying additions to Fe.[27,34] Nevertheless, these freeze-cast structures degrade during cycling due to the collapse of the lamellar structure due to buckling, contact, and sintering between neighboring lamellae, as well as flaring of lamellar tips resulting in the formation of a dense shell encapsulating the structure, as also seen in packed powder beds.[35,36]

The above strategies can be combined to increase degradation resistance of porous Fe structures. Freeze-cast lamellar structures alloyed with Fe-soluble, redox-inactive metals such as Ni or Co can accelerate the reduction reaction and provide a ductile backbone to provide additional mechanical stability to the lamellae.[26,27,34,37] Alloying with Mo was found to be particularly effective due to the sintering inhibition effect provided by Mo.[32]

Based on our understanding of the degradation mechanisms in freeze-cast lamellar structures, it is useful to now consider other porous geometries. Ink-printed microlattices with long channels are of interest due to their high open porosity, ease of fabrication, and mechanical stability.[38–42] The printed walls can also be made mesoporous and microporous, creating a hierarchical pore structure, which counteracts their much-increased thickness, as compared to freeze-cast lamellae. Such structures have recently shown promise for both structural and functional applications.[43–47] A previous study of foamed Fe lattices [38] showed potential for durability through many redox cycles, though the pure Fe composition resulted in a significant slowing in oxidation kinetics after 10 cycles. The present study examines lattices of two alloys, Fe-25Ni and Fe-25Mo (wt%), created by ink-printing of a foamed suspension, and assesses their structural evolution during redox cycling at 800 °C, for up to 50 redox cycles, with comparisons drawn to freeze-cast lamellar structures of the same compositions.

2. Experimental Section

2.1. Ink Preparation and Printing

Hierarchically-porous structures were obtained by mechanical frothing of an aqueous suspension of 40–50 wt% metal oxide powders with 3 μL g^{-1} hexylamine (99% ACROS Organics) used as an amphiphilic surface modifier followed by 3D ink-extrusion printing, using protocols previously described in the literature [43,44] for pure Fe structures with magnetite Fe_3O_4 (E8840,

DOWA), albeit with additions of either nickel(II) oxide NiO (99%, abcr GmbH), or molybdenum(VI) oxide MoO_3 (99.97%, Sigma-Aldrich). The Fe-Ni oxide slurries contained an active metal loading of 77 wt% Fe_3O_4 and 23 wt% NiO, and the Fe-Mo oxide slurries contained an active metal loading of 74 wt% Fe_3O_4 and 26 wt% MoO_3. After reduction, these correspond to Fe-25Ni and Fe-25Mo, wt% (i.e., Fe-24Ni and Fe-16Mo, at%) compositions, with comparable bulk densities of 8.1 and 8.3 g cm^{-3}, respectively.

After initial fabrication, the metallic lattices contain a significant amount of Fe_3Mo_3C and Mo_2C due to reaction with the carbon produced from burnout of organic slurry components during the thermal reduction step. To eliminate these carbides, the lattices were pre-treated via a first redox cycle at 800 °C: oxidation for 90 min under 120 sccm flowing H_2O, then reduction for 90 min under 200 sccm flowing H_2. The final Fe-24Ni metallic lattices had an average mass of 0.44 g, and the final Fe-16Mo metallic lattices had an average mass of 0.34 g; variations stemmed from defects during printing.

2.2. Redox Cycling and Characterization

Redox performance of foamed lattices was studied via consecutive steam and hydrogen exposure (redox cycle) to simulate operating conditions. All cycling was performed in a horizontal alumina tube furnace (61 cm length, 19 mm inner diameter, 25 mm outer diameter, Lindberg Blue Mini-mite) fed via stainless steel tubing by either H_2 (UHP, Airgas) for reduction, or H_2O carried by Ar (UHP, Airgas). H_2O was generated by bubbling the Ar through a vessel of water heated to 93 °C. Gas flow was controlled by two mass flow controllers (MKS). Specimens were placed on an alumina plate in the hot zone, and ramped to 800 °C at 10 °C min^{-1} under flowing H_2 (100 sccm) to maintain the metallic state of the material. After the furnace equilibrates at 800 °C, the first oxidation half cycle begins, where Ar is flowed (120 sccm) through the 93 °C water bubbler, achieving a H_2O steam partial pressure of 78 kPa. All gas lines were heated to 110 °C to prevent any steam condensation. After the first 120 min oxidation half-cycle, pure H2 is flowed (200 sccm) for 90 min for the reduction half-cycle. Subsequent cycles are repeated with 90 min of oxidation, followed by 90 min of reduction: these cycle durations are chosen to ensure full oxidation and full reduction for the initial state, though in later cycling degradation in the lattice can result in incomplete oxidation or reduction due to loss of porosity (discussed in Section 3). Following the last reduction cycle, specimens are cooled at 5 °C min^{-1} under flowing H_2 (100 sccm) to maintain the metallic state after cooling. When a lattice is partially cycled (i.e., when cycling is interrupted before the end of the reduction half-cycle), it was instead cooled under flowing Ar-4% H_2 to prevent further oxidation while maintaining any oxide present. Specimens are weighted after cycling to calculate oxygen gains (if in an oxidized state), or to ensure that no oxide remains (if in the reduced state).

After cycling, foamed lattices were vacuum-mounted in epoxy (Epothin 2, Buehler), and polished to halfway through their height. The final polishing step of the full radial cross-section is done with a 1 µm diamond suspension. For partially or fully oxidized specimens, an additional ion milling step on a LEICA TIC3X is performed to remove polishing damage to the brittle and fragile oxidized layer and to reveal internal porosity. The radial cross sections were imaged on an optical microscope (MA200, Nikon), by stitching together multiple 5x magnification images. The microscope is refocused every four pictures. To analyze the cross-section, the images are processed using the ImageJ software. First, the cross-section is converted to a binary image, with solid treated as 1 and pores as 0. Lattice porosity was calculated from solid fraction, taken as the ratio of solid area to total sample area. Ligament size was calculated by deploying the local thickness algorithm in ImageJ.[43] Pore size is calculated via the local thickness plugin on the inverse of the filtered image described above.

Scanning electron microscopy (SEM) and energy-dispersive X-ray spectroscopy (EDS) imaging were performed on Hitachi 8030 SEM instrument. Epoxy-mounted cross-sections were sputter-coated with a 10 nm Au-Pd film, while unmounted foamed lattices were imaged without coating.

X-ray diffraction (XRD) spectra were gathered in reflection geometry on the polished surface of epoxy-mounted samples. Measurements were performed at room temperature with a Rigaku Smartlab 3 kW instrument with Cu source, operated at 40 kV and 35 mA. Processing of collected spectra was done in Python, and background corrections were performed using a modified polynomial fit.[48]

Pore volume, micropore area, and BET surface area measurements were carried out on full foamed lattices before pre-treatment, after pre-treatment, and at 20 and 50 cycles. These measurements were performed at the Reactor Engineering and Catalyst Testing core facility at Northwestern University. The lattices were first degassed according to ASTM D4222 at 100 °C under vacuum for 24 h, then subsequently tested for N_2 adsorption/desorption at the boiling point of liquid N_2 according to ASTM D4222-03 with a pore structure analysis instrument (Micromeritics 3Flex).

3. Results and Discussion

3.1. Initial Hierarchical Porous Architecture

The printing process is shown schematically in **Figure 1**a: a nozzle deposits the ink, which consists of a mixture of Fe_3O_4 (red), either NiO or MoO_3 (blue) depending on composition, and gas bubbles (white). Each ink-printed 9 × 9 × 8 mm specimen consists of a lattice of 5 × 5 × 16 orthogonal *inner walls* (0.6 mm in diameter) defining 4 × 4 = 16 longitudinal channels, referred to as *channel pores* (Figure 1b); the transverse directions contain no channels, with the 16 layers (Figure 1c, orange arrows) in contact with each other forming a continuous *outer wall* surrounding four of the six faces of the nearly cubic specimens (Figure 1c). The multichannel structure chosen for this study provides gas access to a relatively large lattice, such that the microstructures observed within the struts of the lattice can be compared at multiple different areas within the same lattice. As the structure evolves during cycling, the channels are expected to remain open for gas access, again so that microstructural changes can be observed in multiple areas in a single lattice. While a relatively simple geometry was printed here to compare to lamellar wall structures from freeze-cast foams, ink-printing allows for much more complex architectures.[39,41]

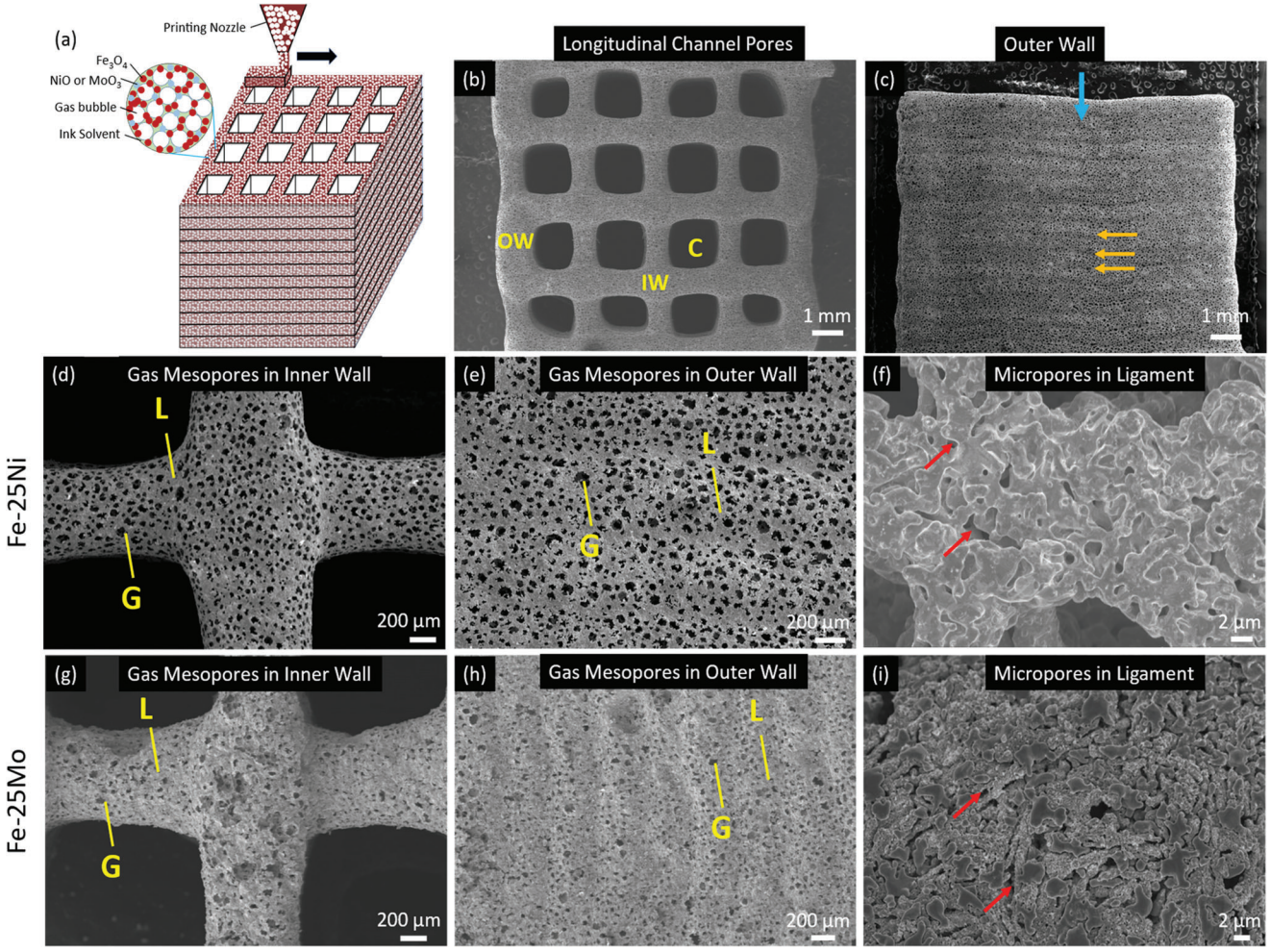

Figure 1. a) Schematic of the printing process, wherein foamed ink (a suspension of Fe_3O_4 (red) and either NiO or MoO_3 (blue) particles with bubbles) is 3D-extruded to form a lattice, which consists of 5 × 5 inner walls forming 16 longitudinal channels. b) Low-magnification SEM micrograph showing the hierarchical porous architecture of the foamed lattices after initial reduction, sintering, and pretreatment: view of channels (C), printed inner walls (IW), and printed outer wall (OW) containing gas mesopores, for Fe-24Ni foamed lattice. c) View of printed outer wall: orange arrows indicate examples of separate printing layers, blue arrow marks the longitudinal view shown in the previous pane. d,e) Medium magnification view of Fe-24Ni inner wall and outer wall, respectively, with gas mesopores (G) and ligaments (L) viewed from the longitudinal and transverse directions, respectively. f) High magnification view of Fe-24Ni ligament micropores (red arrows) within a ligament. g,h) Medium magnification view of Fe-16Mo inner wall and outer wall, respectively, with gas mesopores (G) and ligaments (L) viewed from the longitudinal and transverse directions, respectively. i) High magnification view of Fe-16Mo ligament micropores (red arrows) and two-phase microstructure within a ligament.

The printed walls are also highly porous internally due to the foaming process prior to, and during, ink printing, with a fully interconnected mesoporous structure, referred to as *gas mesopores* (Figure 1c,d). Finally, each Fe-24Ni *ligament* between these foaming pores contains microscale porosity, formed by the escape of H_2O during initial reduction of the oxide powders and present through the subsequent carbide-removal redox pre-treatment, which are referred to as *ligament micropores* (Figure 1e). The structure of the Fe-16Mo gas mesopores (Figure 1d,g) and ligament micropores (Figure 1e,h) is similar. These three length scales of porosity – millimeter-scale channel pores, 20 µm-scale gas mesopores, and 1 µm-scale ligament micropores – form a hierarchical porous structure which is beneficial to maintaining gas access during redox cycling.

The three length scales of solid – wall, ligament, and micro-ligaments – keeps diffusion distances low from any point in the solid to a free surface, lowering the time needed for full oxidation/reduction. The hierarchical porosity also enables ingress of reaction gases (H_2O on oxidation and H_2 on reduction) and egress of product gas (H_2 on oxidation and H_2O on reduction), preventing gas entrapment.

3.2. Fe-24Ni Lattice Evolution

The evolution of Fe-24Ni lattices during the first 20 redox cycles is illustrated in **Figure 2** through representative cross-sections of full specimens, with corresponding SEM micrographs of cross sections of the foamed walls in the lattice interior and at its

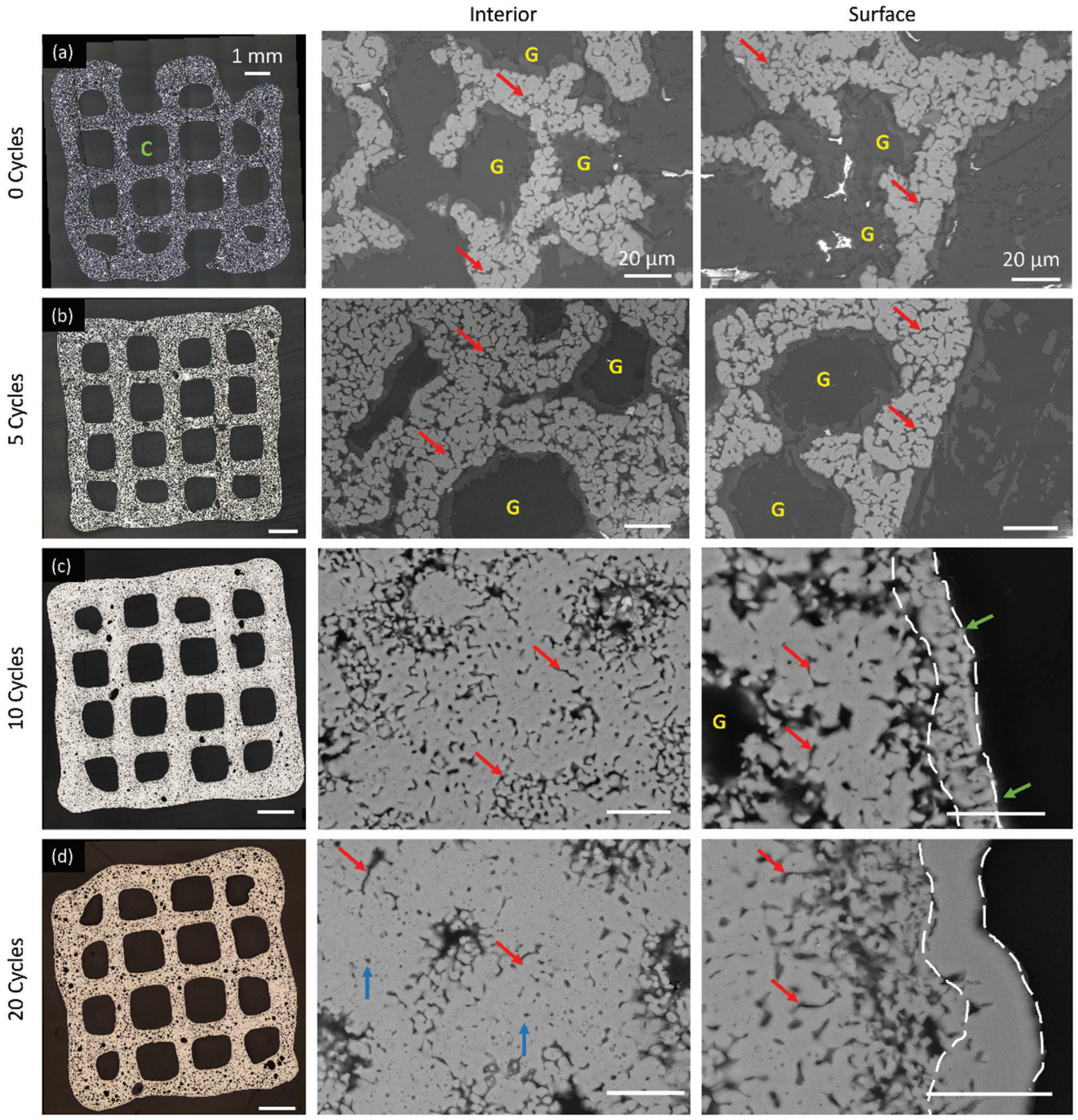

Figure 2. Macro- and micro-structural evolution of Fe-24Ni foamed microlattices shown via polished cross sections at a) 0, b) 5, c) 10, and d) 20 cycles, for (left column) full specimen cross section (optical micrograph, with 1 mm scale bar) showing 4 × 4 longitudinal channels (one is marked C) and 5 × 5 transverse walls; (middle column) cross-section of an interior wall (SEM micrograph, 20 µm scale bar) showing gas mesopores (marked G) and micropores (red arrows); (right column) wall surface cross-section (SEM micrograph, 20 µm scale bar) with a dense outer shell outlined in white to guide the eye. Green arrows mark gas channels through the shell, and blue arrows mark spherodized pores.

surfaces. Occasionally, defects in the printing process appear as missing wall segments, as seen in Figure 2a (left column). The initial wall microstructure consists of Fe-24Ni ligaments separating gas mesopores (yellow letter G), with each ligament containing a microporous network. Initially the interior walls (Figure 1a, middle column) and surface walls (Figure 2a, right column) are identical as no sintering or volume shrinkage has occurred yet in the specimen.

During cycling, mesopores gradually shrink due to the cyclic expansion and contraction of the surrounding solid: During oxi-

dation by steam, Fe oxidizes first to FeO and then to Fe_3O_4, with a 110% molar volume expansion. This brings neighboring regions across the pores into contact, which then sinter irreversibly, both when oxidized and, to a greater degree, during reduction.[5] As a result, the corresponding volumetric contraction during reduction does not return the pore to its initial geometry. Instead, each closed pore is filled with sintered Fe which forms an increasingly dense network as this process repeats.

The role of Ni is to provide a metallic backbone that does not participate in the redox reaction. As shown in a previous study of freeze-cast Fe-24Ni specimens, Ni stabilizes the metallic lamellae by adhering to the Fe_3O_4 layer in the oxidized state, then providing a solid solution into which the freshly reduced Fe can dissolve on subsequent reduction, so that neighboring lamellae are less likely to sinter during their individual volumetric expansion and contraction. Metallic Ni additionally provides a kinetic acceleration of the H_2 oxide reduction at the metal-oxide interface.[26,28,34] Ni does not oxidize under steam, and previous investigations showed that the ternary oxide $NiFe_2O_4$ does not form.[26,34] During oxidation at 800 °C, 12 mol% Fe remains in solid solution with Ni, unable to oxidize; the measured oxidation degree is based on this theoretical weight gain assuming 88 mol% of Fe converted to Fe_3O_4.

Through 5 cycles (Figure 2b), the foamed lattice retains porosity at the channel, gas mesopore, and ligament micropore levels, but at 10 cycles (Figure 2c) and beyond the micropores (red arrows) and gas mesopores (yellow letter G) have densified significantly, especially at the surfaces of each wall, as shown in Figure 2c,d (white outlines). A dense shell forms, most probably due to poor adhesion between the Fe_3O_4 and metallic Ni backbone as observed in lamellar Fe-Ni foams[26,34] in each cycle, this outer shell becomes increasingly depleted in Ni, eventually losing diffusional contact with the Ni backbone.[26] The oxidized surface microstructure is shown in Supplementary Figure S2, Supporting Information initially the oxide contains significant ligament microporosity due to the microporous network left by escaping H_2O, but after 20 cycles no ligament microporosity remains at the surface.

Localized densification at the wall surface is particularly deleterious as the dense outer shell, characteristic of the shrinking core model reduction of iron oxides, blocks gas access to the foamed, porous walls. As a result, loss of redox activity does not occur linearly with densification of the walls, it depends strongly on the thickness and porosity of their outer layer. At 10 cycles, the outer shell is still relatively porous, with gas channels seen even in cross-section (Figure 2c, green arrows). At 20 cycles, however, the shell is fully dense (Figure 2d, white dashed area).

Although the metallic Ni phase stabilizes the structure during oxidation, the propensity of the Fe-24Ni solid solution to rapidly sinter pores slows redox kinetics over time.[26,34] This is because the microporous network within each wall, maintained during cycling by the egress of exhaust steam, is either sintered closed completely or spherodized (Figure 1d, blue arrows). This mechanism contributes to the densification of the walls, as gas cannot quickly flow to their interior lattice with the microporous network sintered closed. The closing of the microporous network can be seen in the large drop in microporosity between 10 cycles (Figure 2c) and 20 cycles (Figure 2d). This coincides with a similar loss in microporosity for the outer shell, resulting in much slower redox kinetics for further cycling. After 20 cycles, a 90 min oxidation period results in just 11% oxidation of the sample, by mass, as compared to 82% after 10 cycles.

As shown in **Figure 3**, cross-sectional micrographs with corresponding EDS maps of the foamed lattice after 20 cycles reveal an interesting trend areas of the lattice walls surrounding the mesopores are Ni-poor, while areas further from mesopores and other surfaces are closer to the expected Fe-24Ni composition. Correspondingly, Ni-rich areas are much denser, while the Ni-poor areas, close to mesopores, are more microporous, with the exception of the outer shell (which contains no Ni and little microporosity). This microstructure is evidence of segregation similar to that observed previously for Fe-Ni freeze-cast foams.[26,34] During oxidation, Fe atoms diffuse to the surface to oxidize; in the Fe(Ni) solid solution, Ni atoms balance this mass flux and diffuse inward, resulting in a characteristic Ni-rich core / Fe oxide shell structure. Delamination between shell and core can inhibit the diffusion of Fe back into the Ni core, however, resulting in phase segregation in the reduced state between Ni-poor, porous, outer areas (where the microporosity has increased diffusion distance inwards), and Ni-rich, dense inner areas, where the Ni remained during oxidation (thus having more time to sinter micropores closed). This segregated microstructure is evidence of both the self-healing effect of Ni on the lattice (which, in this case, is detrimental as it reduces porosity) and of a lack of diffusional pathways for Fe in porous areas to diffuse back to the interior of the wall.

3.3. Fe-16Mo Foamed Lattices

3.3.1. Microstructural Evolution of Fe-16Mo Lattices

Fe-16Mo foamed lattices evolve in a more complex manner during cycling due to the multiple phases present in both the oxidized and reduced states. To address this complexity, we first discuss the microstructural evolution of the lattice, then relate those microstructural factors to bulk changes in the lattice pore structure and to the surface evolution. As discussed in more details below, the redox cycling results in first a relatively rapid homogenization of the initially highly segregated microstructure, followed by a slower segregation of Mo into dense, slow-reacting agglomerates. Throughout this process, however, the porous wall remains able to oxidize to 92% of the maximum value and to subsequently reduce completely to the metallic state.

The Fe-16Mo lattice, as shown in **Figure 4**a after pretreatment, consists of a two-phase mixture of bcc Fe with ~4 at% Mo in solid solution (green letter F) and λ-Fe_2Mo (orange letter M), as also reported in lamellar foams of the same composition.[32] The bcc Fe phase (white dashed region), which makes up a majority of the volume of the walls, consists of larger, meso-scale domains displaying small amounts of microporosity. The Fe_2Mo Laves phase (yellow dashed region) consists of micro- and nanoscale domains consistent with the CVT reduction mechanism that controls MoO_2 and $Fe_2Mo_3O_8$ reduction. The smaller size of the Fe_2Mo regions is also indicative of the sintering inhibition effect from Mo, as neighboring intermetallic regions do not sinter together quickly. These phases can be distinguished by z-contrast in the electron images in Figure 4, with the bcc Fe phase

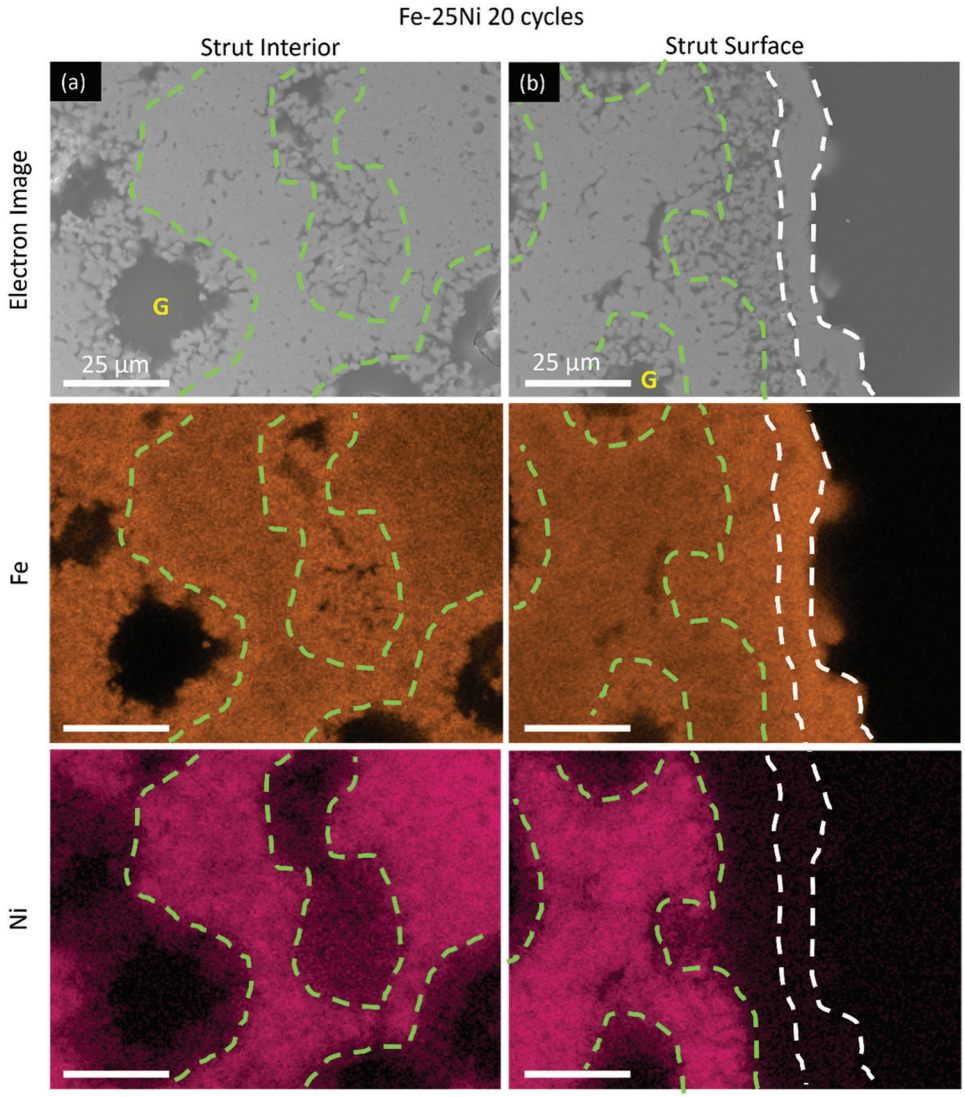

Figure 3. SEM micrographs of cross-sections of representative foamed walls after 20 redox cycles with corresponding EDS maps for Fe (orange) and Ni (pink) for a) the wall interior and b) the wall surface. Green dashed lines guide the eye for the demarcation between the Ni-rich region (inside green dashed lines) which are denser, and the Ni-poor region (outside green dashed lines), which are more microporous.

appearing dark gray and the intermetallic, Mo-rich phase appearing light gray/white. Phase composition was confirmed by XRD, shown in Figure S3, Supporting Information.

Both Fe and Mo can be oxidized by steam at 800 °C. In this system, three phases are formed, shown in Figure 4b, Fe_3O_4 (green letter F), and a mixture of MoO_2 and $Fe_2Mo_3O_8$ (orange letter M). While the Mo-containing phases are difficult to distinguish with EDS, it is assumed that the mixed oxide forms at the interface of Mo-rich and Fe-rich regions, while MoO_2 forms at the center of Mo-rich regions, particularly as segregated Mo-rich regions grow in size. Phase composition was confirmed by XRD, shown in Figure S3, Supporting Information.

The distribution of these phases is shown in Figure 4a (right). Unlike the Fe-24Ni wall microstructure, the interpenetrating, multiphase structure in the oxidized state prevents the Fe_3O_4 from coarsening, as each Fe_3O_4 domain is closely bordered by MoO_2 and $Fe_2Mo_3O_8$, preventing diffusion and sintering in the microstructure.

After 10 cycles, the reduced microstructure (Figure 4c) is similar to the initial state, albeit with a shrinkage in the mean gas mesopore size. There is a clear separation between Fe-rich bcc (white dashed region) and Mo-rich Fe_2Mo (yellow dashed region). The oxidized microstructure (Figure 4d) shows some homogenization, with $Fe_2Mo_3O_8$ and MoO_2 regions extensively interspersed in Fe_3O_4 regions (red arrow), rather than remaining fully segregated. This indicates that the cycling has a homogenizing effect on the microstructure: as the Fe-rich regions expand (on oxidation) and contract (on reduction), they may envelop neighboring Mo-rich domains due to the higher volume fraction of Fe_3O_4 in the wall; this behavior is reminiscent of that observed in redox cycling of lamellar Fe foams containing stainless steel bridging fibers, where the Fe cyclically accumulates on nearby non-Fe phases during cyclical expansion and contraction.[49] This ef-

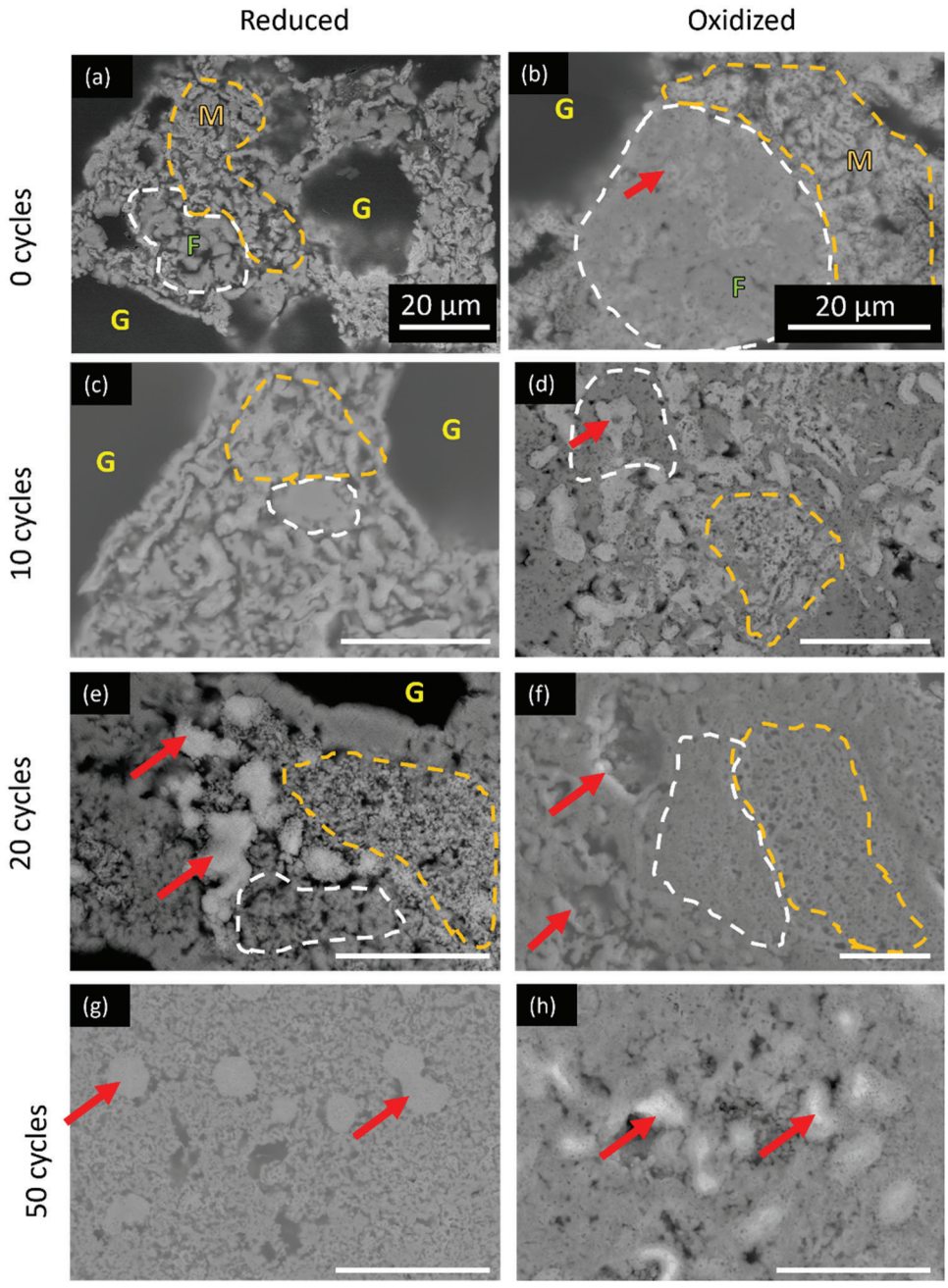

Figure 4. SEM micrographs of Fe-16Mo foamed microlattice wall cross-sections with 20 µm scale bar at a,b) 0, c,d) 10, e,f) 20, and g,h) 50 cycles in the reduced (left column) and oxidized (right column) states. Red arrows mark Mo agglomerates. Yellow and white dashed areas mark Mo-rich and Fe-rich microporous regions, yellow letter "G" marks gas mesopores, green letter "F" marks Fe-rich phase, orange letter "M" marks Mo-rich phase.

fect, combined with the overall shrinkage of the foamed walls resulting in loss of mesoporosity, brings the two phases into closer contact, resulting in improved dispersion of the Mo in the lattice walls. Regions with high Mo content and relatively small MoO_2 domain size (yellow dashed region) also show increased microporosity, probably due to enhanced sintering inhibition.

Between 10 and 20 cycles, the reduced microstructure changes significantly (Figure 4e). Most gas mesopores larger than 10 µm have shrunk to a smaller size, though the microporous network within each wall remains open and fully connected. Histograms showing the pore size distribution are provided in Figure S4, Supporting Information. The most striking development is the growth and shape change of the large Mo-rich regions in the lattice (Figure 4e). They were originally elongated and relatively small (1 µm width), as seem in (Figure 4a and Figure 2b), but after redox 20 cycles, they have coarsened to 2–3 µm in width and begun to spherodize. These Mo-rich regions also no longer show porosity at their center, indicating the Mo within them is

no longer undergoing cyclical redox reactions. These morphological changes correspond to the appearance of bcc Mo peaks in the XRD spectra (Figure S3, Supporting Information), indicating that these Mo-rich regions are fully segregated from the surrounding Fe matrix.

The foamed walls at 20 cycles are Mo-rich in some areas (Figure 4e, yellow dashed area) and Mo-poor in others (Figure 4e, white dashed area). Both regions have significant microporosity, however, indicating that, even in Mo-poor areas, the Mo content is sufficient to inhibit sintering. The oxidized state (Figure 4f) contains the same features, but with a smaller micropore size due to filling from the volume expansion during oxidation, but the foamed walls remain porous and able to oxidize to 92% in 90 min steam exposure.

The segregation of Mo follows two distinct transport pathways that decrease interactions between Mo and Fe. Within walls, Mo-rich aggregates form and gradually coarsen with additional cycling. The transport of Mo is accelerated during the reduction of MoO_2 and $Fe_2Mo_3O_8$: for these oxides, the reduction is expected to proceed via chemical vapor transport mechanism, in which vapor phase $MoO_2(OH_2)$ forms in the vapor phase before condensing as pure α-Mo.[29–31] Once condensed, the nascent α-Mo will react with Fe to form Fe_2Mo; however, as Fe coarsens at the exterior of the wall, there will be less Fe distributed within the wall to react and form Fe_2Mo. Mo that is unable to form Fe_2Mo will instead coarsen via bulk and surface diffusion to form the Mo-rich aggregates observed in Figure 4.

Once coarsened, the Mo-rich aggregates can be considered as unreactive regions, since the relatively slow kinetics of oxidation and reduction of densified Mo prevent these aggregates from contributing substantially to the overall redox response of the sample. Additionally, these aggregates no longer provide sintering inhibition to the surrounding matrix as they have limited interaction with Fe.

At 50 cycles (Figure 4g), the major changes in the reduced microstructure are: (i) Mo-rich microporous areas are no longer common in the bulk of the lattice and (ii) Mo aggregates have further coarsened (to 4 μm width when reduced) and they are increasingly spherical in shape. No Fe-rich aggregates are observed in the wall interiors, though an Fe shell has formed (as discussed below). The oxidized microstructure (Figure 4h) closely resembles the reduced microstructure, albeit with lowered porosity; however, the lack of reactivity in the center of the Mo-rich agglomerates is clearly seen from the z-contrast: the centers are bright white, indicating high Mo with little to no O or Fe present. However, the lattice walls remain porous in both the reduced and oxidized state, allowing for 92% oxidation and 98% reduction in the 90-min half cycles.

3.3.2. Surface Evolution of Fe-16Mo Lattices

Shell formation at the wall surfaces, due to the net diffusion of Fe outwards during oxidation combined with irreversible sintering of Fe_3O_4 regions that come into contact, occurs in Fe-16Mo lattices as well, though the sintering inhibition provided by Mo prevents this shell from becoming fully dense as in Fe-24Ni. Images of the wall surface in the reduced and oxidized states are shown in **Figure 5**. At 10 cycles (Figure 5a) a shell is visible, though it is not yet fully formed: regions of Fe aggregation are observed on the surface of the underlying microporous walls. Large pores (yellow arrows) are frequent throughout the wall surface. In the oxidized state (Figure 5d), a highly porous Fe_3O_4-rich shell covers the wall surface. The inset in Figure 5d reveals that this shell consists of oxide grains ranging in size from 1 to 10 μm, with little contact between neighboring grains. Some larger cracks (green highlight) are observed as well.

At 20 cycles in the reduced state (Figure 5b), an Fe-rich shell covers most of the wall surface. However, wide cracks cut through the shell frequently, exposing the porous interior of the wall, so that the shell does not slow the kinetics of the reaction, as gas can easily reach the microporous interior. Gas mesopores (yellow arrow) remain connected to the surface as well, providing another easy path for gas access to the microporous wall interior.

Similarly, in the oxidized state (Figure 5e), the fully formed shell contains large pores (yellow arrows) as well as smaller pores and cracks (inset, green arrows) that allow gas to pass through and react with the interior. In some regions, high Mo content also leads to the formation of intergranular MoO_2 and $Fe_2Mo_3O_8$ (Figure 5e, blue regions) that suppress shell connectivity, or a surface consisting entirely of porous MoO_2 and $Fe_2Mo_3O_8$. Higher magnification views of these features are shown in Figure S5, Supporting Information.

At 50 cycles (Figure 5c), the wall shell has undergone further transformation, as more micropores have developed in its surface. This is expected to occur through the continuing diffusion of Mo throughout the lattice because of the concentration gradient created via the continual depletion of Mo at the wall surface due to chemical vapor transport.[29] The oxidized shell (Figure 5f) is similar to that at 20 cycles, with cracks occurring at both the a larger, wall-length scale (Figure 5f, green region) and at a smaller, intergranular scale (Figure 5f inset, green region). Gas mesopores open to the surface are no longer common.

The wall surface microstructure after 50 cycles, shown in cross-sections in **Figure 6** for the reduced and oxidized states, reveals an additional mechanism of degradation. In this area, Mo appears to be completely removed from the specimen through the formation of the vapor phase $MoO_2(OH)_2$,[29,30,50] consistent with the observation of Mo deposits on the furnace tube. This is shown both by the total lack of Mo at the outer surface of the wall in the oxidized state (Figure 6b) and through the gradual mass loss during cycling of each specimen. After 50 cycles, an average mass loss of 4.75% is measured, corresponding to a loss of 29% of the initial Mo content, assuming no mass loss from other sources (such as spalling). This degradation mechanism could be prevented by lowering the temperature of operation, which would however slow the reaction kinetics.

These mechanisms lead to distinct regions in the oxidized microstructure near the wall surface after 50 cycles, as shown in Figure 6 Mo-rich aggregates (red arrows), a microporous, two-phase oxide mixture (region III), a mesoporous Fe-rich phase (region II), and a Fe_3O_4 shell (region I). Further inside the walls, far from the surface, the microporous microstructure and the Mo-rich agglomerates are observed. In the reduced state, the distinction between regions II and III is not as clear; rather, a homogenous mixture of Fe and Mo is observed between micron-scale Mo-rich regions. The shell is now a Fe-rich layer at the surface of the wall, which is not fully dense in the reduced state (due to

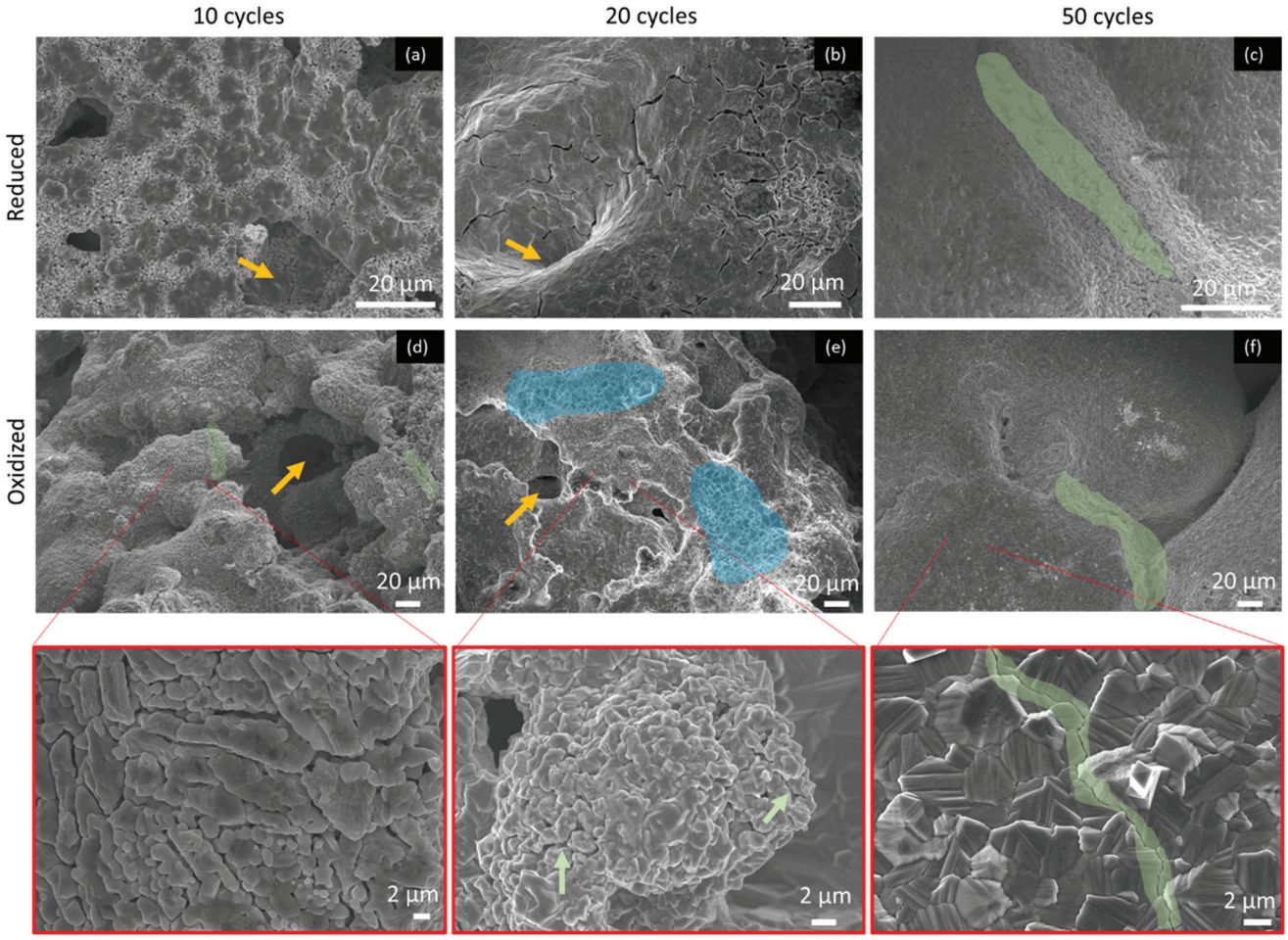

Figure 5. SEM micrograph of Fe-16Mo microlattice wall surfaces illustrating shell formation after a) 10 cycles, b) 20 cycles, and c) 50 cycles in the reduced (a-c) and oxidized d–f) states. High magnification views (bottom row) show intergranular fracture in the oxidized shell. Green arrows and green bands highlight cracks. Yellow arrows mark gas mesopores. Blue regions highlight mark Mo-rich regions.

the cracks and pores discussed in Figure 5), allowing gas to reach the microporous interior wall volume.

The EDS mapping shown in Figure 6 raises the question why, since the surface of the wall is devoid of Mo, does the Fe_3O_4 region not sinter into a fully dense shell as in the Fe-24Ni lattice. As shown previously in Figure 5, cracking is common in the oxidized state. These cracks appear to be crucial in preventing the sintering of the outer shell. These cracks do not heal during the cyclic expansion and contraction of the walls, and the difference in molar volume expansion and contraction between the outer, mostly dense Fe to Fe_3O_4, and the underlying porous Fe/Fe_2Mo mixture to $Fe_3O_4/Fe_2Mo_3O_8/MoO_2$ is probably sufficient to reopen cracks each cycle, up to 50 cycles. Continued cyclability is expected given the slow rate of densification through 50 cycles, though the depletion of Mo in the lattice will eventually result in accelerated degradation.

The retention of micropores in the walls of the lattice, which is vital to the continued reactivity of the specimens, is due in part to the cyclical regeneration of pores during the reduction of MoO_2 and $Fe_2Mo_3O_8$. Since these phases reduce via chemical vapor transport, the resultant Fe_2Mo grains are nanocrystalline.[31,51] Because this phase is cyclically recrystallized with some degree of submicron porosity between the nanocrystalline grains after each reduction, sintering of pores is inhibited and new pores are introduced each cycle. Evidence of this process is seen also in BET surface area measurements summarized in **Figure 7**, with full adsorption data available in Figure S6, Supporting Information.

3.3.3. Macroscopic Changes in Fe-16Mo Lattices

Macroscopic changes in the Fe-16Mo lattices are shown in **Figure 8** for the surface (left) and interior (right) of walls after (a) 0, (b) 10, (c) 20, and (d) 50 redox cycles. The initial foamed lattice architecture is very open, with hierarchical porosity of millimeter channel pores, 20 µm-scale gas mesopores (yellow arrows), and microscale pores between different phases. After 10 cycles, the overall porosity decreases as the lattice shrinks, though the same hierarchy of pore size is observed. After 20 cycles, the lattice continues to shrink, and many of the gas mesopores have disappeared. After 50 cycles, these gas mesopores are even rarer.

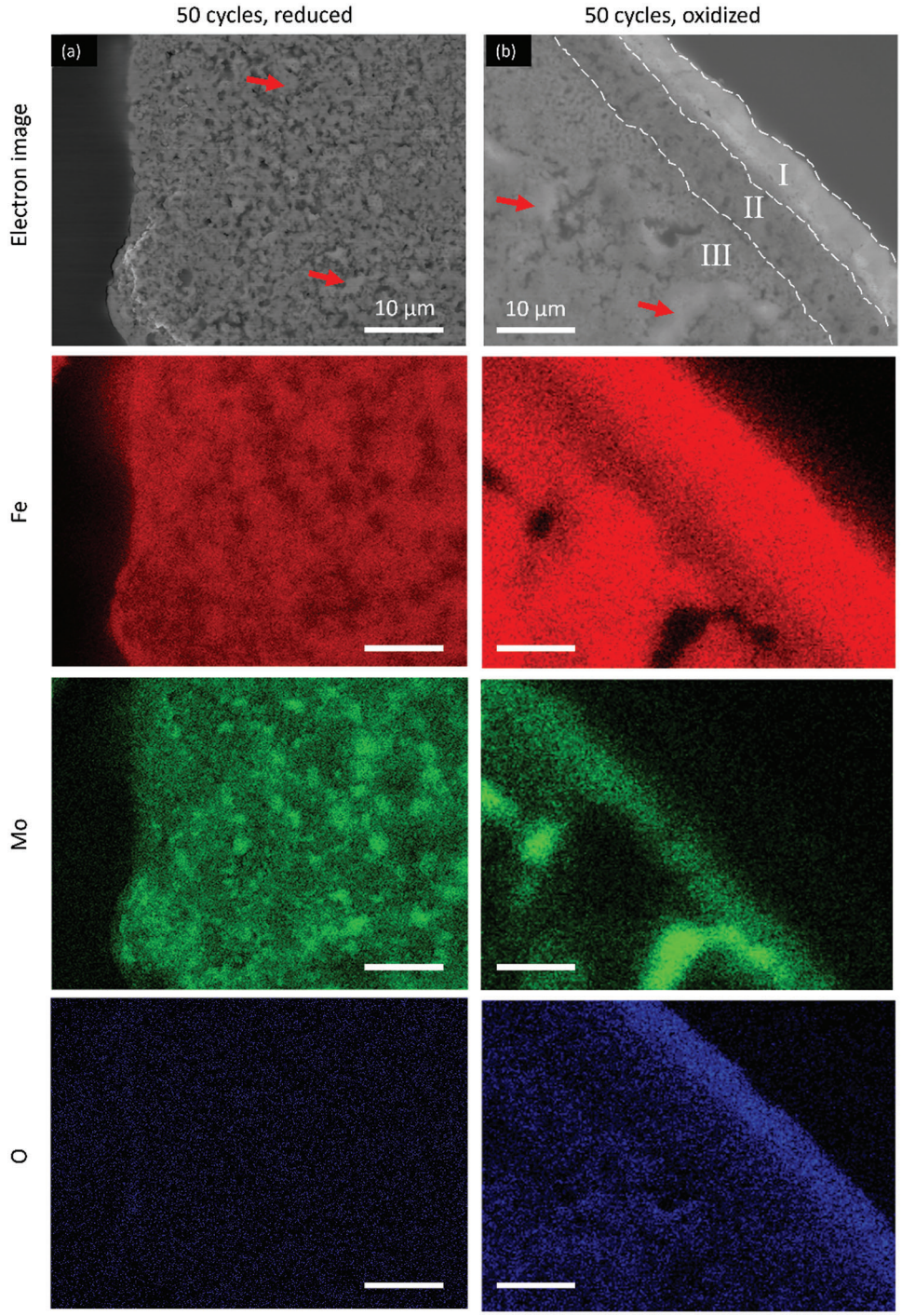

Figure 6. SEM micrographs and corresponding EDS maps (for Fe, Mo, and O) of a representative Fe-16Mo microlattice wall cross-section after 50 cycles in the a) reduced and b) oxidized states. Red arrows mark Mo agglomerates. The dashed lines in (b) guide the eye for three regions of distinct microstructure: I. densified Fe_3O_4 shell, II. Porous Mo-poor lattice and III. Mo-rich microporous ergins.

The wall surface is significantly less porous, though as previously seen in Figure 5f, substantial microporosity is present. At 10, 20, and 50 cycles, large cracks can be seen in the specimen surface (green arrows). In the absence of gas mesopores, as is the case after 50 cycles, these cracks expose the porous wall interior to gases allowing for reactivity even after severe densification.

Fe-16Mo foamed lattices are more prone to local collapse after sintering, as shown by missing wall segments in Figure 8, right column. This is due to the lower mechanical stability of the less-sintered, mixed-phase microstructure, sometimes resulting in failure when handling the specimens. These defects are not expected to influence the overall redox behavior of the lat-

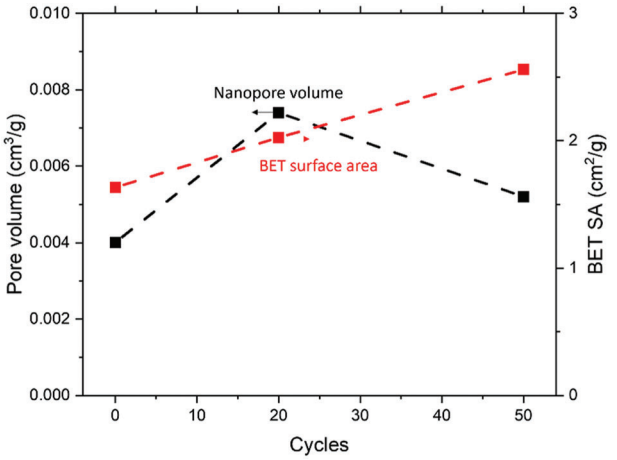

Figure 7. Evolution of pore volume and BET surface area with redox cycle number for Fe-16Mo microlattices, as measured in the reduced state.

tice, and they are excluded from measurements of macroscopic porosity these defects will affect the mechanical properties of the various lattices, which is however beyond the scope of this study.

From the cross-sectional images, five microstructural parameters of the foamed lattices are measured to assess its degradation with cycling: (a) overall porosity (including contributions of channel pores, gas mesopores, and ligament micropores), (b) wall porosity (overall porosity excluding the millimeter-scale channel pores), (c) mean ligament size, (d) mean pore size (excluding large channels), and (e) mean channel size. These parameters are reported in **Figure 9** for both Fe-24Ni and Fe-16Mo compositions.

Figure 9a shows that, whereas both foamed lattices start with the same initial porosity, the Fe-24Ni lattices initially lose porosity much faster than the Fe-16Mo lattices, before reaching a steady state corresponding to stable channel size (Figure 9e). For Fe-24Ni, the wall porosity (Figure 9b) continues to decrease, corresponding to the continued increase in ligament size (Figure 9c). The micropore size (Figure 9d) first decreases rapidly as pores pinch off and shrink, but then stabilizes. This is attributed to two factors: first, the remaining pores spherodize, increasing their measured size as compared to a longer, channel-like pore. Second, the pores shrink and disappear by sintering, removing their contribution to the pore size measurement.

The pore evolution is quite different for the Fe-16Mo lattices. Although the porosity and wall porosity decrease (Figure 9a,b), this decrease is much more gradual than in the Fe-24Ni lattice. The micropore shrinkage (Figure 7d) and ligament growth (Figure 9c) are more stable as well, with the average ligament size increasing from 10 to 15 μm in 50 cycles, as compared to an increase from 10 to 60 μm in the Fe-24Ni lattices. The stability in pore size is consistent with the microstructural evolution observed in Section 3.2.1, as the distribution of Mo throughout the walls prevents large-scale sintering in both the reduced and oxidized states.

The channel width (Figure 9e) in the Fe-16Mo lattices continue to decrease linearly throughout cycling, whereas the Fe-24Ni channel width stops decreasing after 10 cycles. This continued decrease is an indication of the continued redox reactivity of the sample, and the lack of a dense, rigid shell around each wall. The formation of this dense shell in the Fe-24Ni lattices contributes to both the lack of reactivity and the halting of further macroscopic shrinkage of the lattice.

3.4. Comparison to Freeze-Cast Lamellar Foams

Previous work has examined Fe-25Ni (at%) and Fe-25Mo (at%) redox cycling in freeze-cast foams consisting of lamellae ~ 20 μm wide, separated by lamellar channels ≈40 μm wide. By comparing our previous findings with the results of this work, we can draw conclusions about the influence of bulk architecture on the structural evolution of these porous materials during redox cycling. While the exact compositions differ between the ink-printed lattices and the freeze-cast foams, the same reactions occur, and the same phases form, allowing for a meaningful comparison between the different architectures.

Figure 10 shows, for these two architectures, the evolution with redox cycling of porosity, envelope volume change (measuring the outer envelope of the sample), micropore size, and ligament/lamella size, as measured through cross-section image analysis. Specimen porosity and envelope volume change are the two measures best used to evaluate the bulk sample change, while the micropore and ligament size reflect microstructural changes at the ligament/lamellar level. The porosity and envelope volume change measurements (Figure 10a,b) clearly show a difference in behavior between freeze-cast lamellar foams and ink-printed foamed lattices: the latter tend to lose porosity and volume at a faster rate than the former. This is because, for a freeze-cast lamellar foam, changes in bulk porosity or volume can only occur when neighboring lamellae buckle, contact each other, and sinter at the contact point otherwise the limited connections between lamellae strongly inhibit mass transport that might result in pore shrinkage. The pore size is important as well: freeze-cast lamellar foams contain highly anisotropic, planar channels separated by thin lamellae, whereas our ink-printed foamed lattices contain fully interconnected walls with spherical pores that can more easily shrink as the solid regions surrounding them sinter. Because the ink-printed lattices are fully 3D interconnected with relatively easy mass transport throughout their volumes, the porosity loss and volume loss are faster as compared to freeze-cast lamellar foams which show a highly anisotropic lamellar structure.

Microstructurally, the two architectures perform similarly. In particular, the ligament/lamella size is quite consistent across both Fe-Mo architectures (Figure 10d). This indicates that the microporous microstructure is maintained regardless of architecture or macroscopic porosity changes. Micropore size (Figure 10c) varies more in the freeze-cast lamellar foams due to the unpredictable pattern of buckling that can emerge (particularly for large freeze-cast lamellar colonies), driving some channels to widen, thus increasing the average value. The high variability of behavior in lamellar foams is clear, especially when compared to the very low variability for the foamed lattices. The discrepancy is greatest for the Fe-25Ni composition, since unpredictable lamellar buckling and sintering results in some freeze-cast foams densifying much faster than others, while the ink-printed foamed lattices are remarkably consistent.

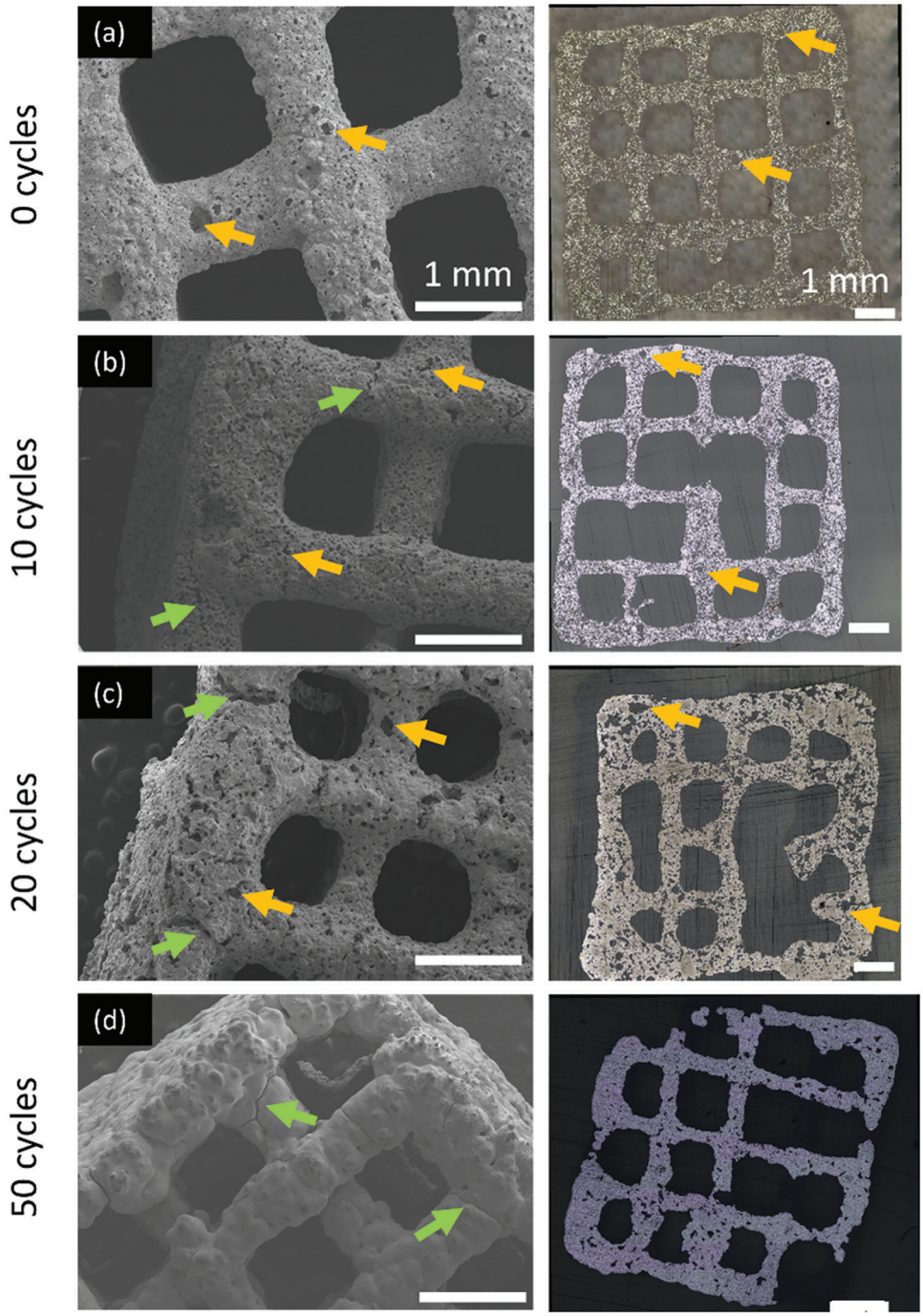

Figure 8. Macroscopic evolution of Fe-16Mo lattices shown at the surface (left) and interior (right) at a) 0, b) 10, c) 20, and d) 50 cycles. Yellow arrows mark gas mesopores. Green arrows mark large cracks in the lattice surface.

An important metric not measured in this study is the mechanical stability of the two porous architectures. Qualitatively, the ink-printed foamed lattices are significantly stronger and easy to handle without damage, increasing their practicality as compared to freeze-cast lamellar foams. A quantitative study of the mechanical properties of the foamed lattice with different composition lies beyond the scope of this study but could be valuable for practical applications of the material.

4. Conclusions

The macro-, meso- and microstructural evolution of Fe-24Ni and Fe-16Mo ink-printed foamed lattices are examined during redox cycling. The lattices contain three distinct pore categories that form a hierarchically-porous architecture: (i) millimeter-scale channels separating walls printed from the ink, (ii) 20-µm scale gas mesopores within printed walls, from the foaming pro-

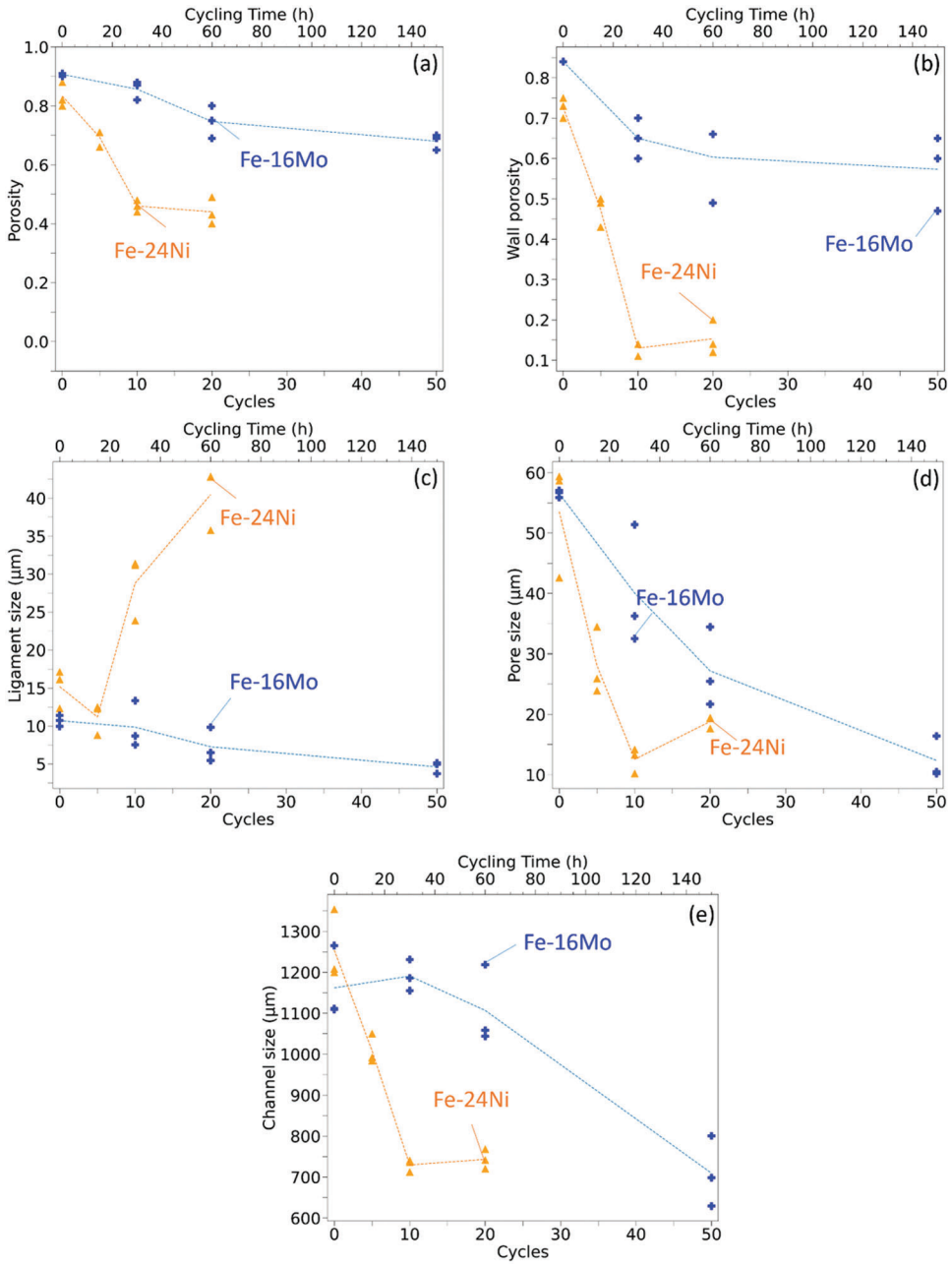

Figure 9. Evolution with redox cycles of microstructure of Fe-24Ni and Fe-16Mo microlattices a) overall porosity, b) wall porosity (excludes channel pores), c) ligament size (excludes channels), d) pore size, e) channel size.

cess within the ink, and (iii) 1-μm scale micropores in ligaments separating mesopores, from the escape of steam/hydrogen during redox cycling.

The rapid sintering behavior of the Fe-24Ni lattices results in densification and sintering of both meso-and micropore networks in the foamed walls, causing the lattices to lose their reactivity, due to choking of gas access, after 30 cycles. By contrast, the Fe-16Mo foamed lattices remain fully reactive up to 50 cycles and open to redox gases, due to the sintering inhibition of Mo and the phases formed. The Fe-16Mo foamed lattices comprise 2–3 different phases: bcc Fe(Mo) and λ-Fe_2Mo in the reduced state, and Fe_3O_4, MoO_2, and $Fe_2Mo_3O_8$ in the oxidized state. The Mo-rich phases prevent local densification by sintering, allowing the micropore networks to remain open, thus enabling ingress and egress of hydrogen and steam during redox cycling. The two-phase microstructure (bcc Fe(Mo) and Fe_2Mo) homogenizes during cycling as the two-phase regions are cyclically brought into contact, resulting in homogeneous microporosity throughout the walls. With continued cycling, this microstructure is generally maintained, though Mo is gradually depleted through both aggregation into slow-reacting, 5-μm wide Mo-rich regions and chemical vapor transport out of the lattice.

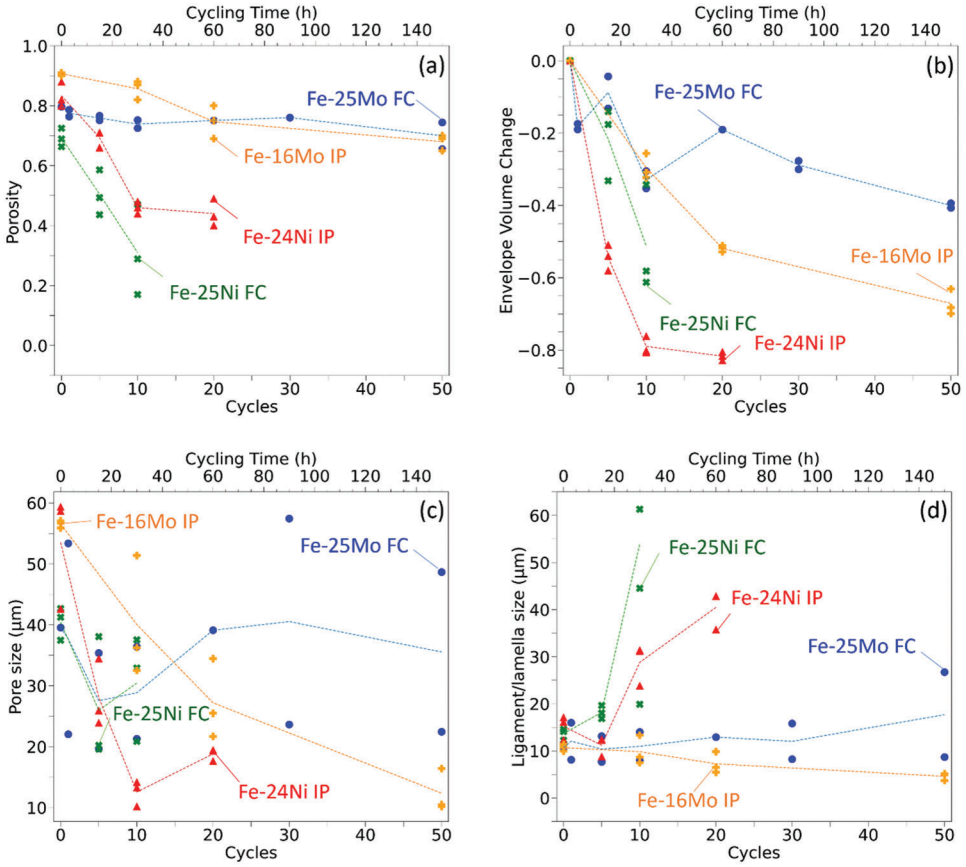

Figure 10. Evolution with redox cycles of microstructure of foams with various architectures a) total porosity, b) envelope volume change, c) micropore size, and d) ligament/lamella size. Data shown for freeze-cast foams (Fe-25Ni and Fe-25Mo[26,32]) and ink-printed foamed lattices (present study) for Fe-24Ni (red) and Fe-16Mo (orange) up to 50 cycles.

The two-phase microstructure of Fe-16Mo foamed lattices also prevents the formation of a fully dense outer shell on its extruded walls: while an Fe-rich shell forms, large cracks (probably caused by mismatch in expansion and contraction of the two underlying phases, Fe and Fe_2Mo) allow full gas access to the porous interior, allowing each wall to remain redox active, even after severe shrinkage. These microstructural effects closely follow those observed in freeze-cast, lamellar foams of the same composition.

Supporting Information

Supporting Information is available from the Wiley Online Library or from the author.

Acknowledgements

The research performed at Northwestern University was funded by the US National Science Foundation under grant CMMI-2015641. Experiments and characterization at Northwestern University made use of the Materials Characterization and Imaging Facility, the NUANCE Center, and the Jerome B. Cohen X-Ray Diffraction Facility (supported by SHyNE under NSF ECCS-1542205, MRSEC under NSF DMR-1720139, the International Institute for Nanotechnology, the Keck Foundation, and the State of Illinois). Prof. André R. Studart (ETH) is acknowledged for useful discussions and use of laboratory facilities at ETH.

Conflict of Interest

DCD discloses a financial interest in Cell Mobility, Inc., a company involved with freeze-casting of metal foams. BC and JAC have a financial interest in Apheros AG, a company commercializing foamed metals.

Data Availability Statement

The data that support the findings of this study are available from the corresponding author upon reasonable request.

Keywords

3D printing, additive manufacturing, energy storage, iron, redox cycling

Received: June 30, 2023
Revised: August 21, 2023
Published online: September 8, 2023

[1] S. Trocino, M. Lo Faro, S. C. Zignani, V. Antonucci, A. S. Arico, *Appl. Energy* **2019**, *233*, 386.
[2] C. Zhang, K. Huang, *Adv. Energy Mater.* **2021**, *11*, 2000630.

[3] X. Zhao, Y. Gong, X. Li, N. Xu, K. Huang, *J. Electrochem. Soc.* **2013**, *160*, A1716.
[4] X. Zhao, X. Li, Y. Gong, K. Huang, *Chem. Commun.* **2014**, *50*, 623.
[5] C. M. Berger, O. Tokariev, P. Orzessek, A. Hospach, Q. Fang, M. Bram, W. J. Quadakkers, N. H. Menzler, H. P. Buchkremer, *J. Energy Storage* **2015**, *1*, 54.
[6] T. Czakiert, J. Krzywanski, A. Zylka, W. Nowak, *Energ.* **2022**, *15*, 1563.
[7] Y. Saito, F. Kosaka, N. Kikuchi, H. Hatano, J. Otomo, *Ind. Eng. Chem. Res.* **2018**, *57*, 5529.
[8] Y. Xiong, J. Zhao, Z. Zheng, W. Li, *Int. J. Hydrogen Energy* **2020**, *45*, 28372.
[9] X. Zhao, N. Xu, X. Li, Y. Gong, K. Huang, *RSC Adv.* **2012**, *2*, 10163.
[10] X. Zhao, Y. H. Gong, X. Li, N. S. Xu, K. Huang, *Mater. Sci. Forum* **2014**, *783–786*, 1667.
[11] H. Lea, G. Bernd, D. Belal, *Proceedings of the International Renewable Energy Storage Conference 2021 (IRES 2021)*, Atlantis Press, **2022**, pp. 126–135.
[12] C. D. Bohn, J. P. Cleeton, C. R. Müller, S. Y. Chuang, S. A. Scott, J. S. Dennis, *Energy Fuels* **2010**, *24*, 4025.
[13] K. Otsuka, T. Kaburagi, C. Yamada, S. Takenaka, *J. Power Sources* **2003**, *122*, 111.
[14] J. Eigen, B. Rutjens, M. Schroeder, *J. Energy Storage* **2021**, *43*, 103161.
[15] N. S. Yüzbasi, P. M. Abdala, Q. Imtiaz, S. M. Kim, A. M. Kierzkowska, A. Armutlulu, W. van Beek, C. R. Müller, *Phys. Chem. Chem. Phys.* **2018**, *20*, 12736.
[16] L. Ma, Y. Qiu, M. Li, D. Cui, S. Zhang, D. Zeng, R. Xiao, *Green Energy Environ.* **2021**, *6*, 875.
[17] E. Romero, R. Soto, P. Durán, J. Herguido, J. A. Peña, *Int. J. Hydrogen Energy* **2012**, *37*, 6978.
[18] X. Zhao, Y. Gong, X. Li, N. Xu, K. Huang, *J. Mater. Chem. A* **2013**, *1*, 14858.
[19] X. Zhao, X. Li, Y. Gong, N. Xu, K. Romito, K. Huang, *Chem. Commun.* **2013**, *49*, 5357.
[20] S. R. J. Saunders, M. Monteiro, F. Rizzo, *Prog. Mater. Sci.* **2008**, *53*, 775.
[21] R. C. Stehle, M. M. Bobek, R. Hooper, D. W. Hahn, *Int. J. Hydrogen Energy* **2011**, *36*, 15125.
[22] P. Charvin, S. Abanades, G. Flamant, F. Lemort, *Energy* **2007**, *32*, 1124.
[23] G. Belton, A. Jordan, *J. Phys. Chem.* **1965**, *69*, 2065.
[24] A. T. Nelson, E. S. Sooby, Y. J. Kim, B. Cheng, S. A. Maloy, *J. Nucl. Mater.* **2014**, *448*, 441.
[25] D. Spreitzer, J. Schenk, *Steel Res. Int.* **2019**, *90*, 1900108.
[26] J. B. Mack, S. M. Pennell, D. C. Dunand, *Acta Mater.* **2022**, *237*, 118148.
[27] S. M. Pennell, J. B. Mack, D. C. Dunand, *J. Alloys Compd.* **2022**, *918*, 165606.
[28] A. R. Puigdollers, P. Schlexer, S. Tosoni, G. Pacchioni, *Increasing Oxide Reducibility: The Role of Metal/Oxide Interfaces in the Formation of Oxygen Vacancies*, American Chemical Society, **2017**, pp. 6493.
[29] W. V. Schulmeyer, H. M. Ortner, *Int. J. Refract. Hard Mater.* **2002**, *20*, 261.
[30] J. Dang, G.-H. Zhang, K.-C. Chou, *High Temp. Materi. Processes* **2015**, *34*, 417.
[31] R. Morales, D. Sichen, S. Seetharaman, I. Arvanitidis, *Metall. Mater. Trans. B* **2002**, *33*, 589.
[32] J. B. Mack, S. M. Pennell, D. C. Dunand, *Acta Mater.* **2023**, 119015.
[33] J. Seuba, S. Deville, C. Guizard, A. J. Stevenson, *Sci. Technol. Adv. Mater.* **2016**, *17*, 313.
[34] S. K. Wilke, D. C. Dunand, *J. Mater. Chem. A* **2020**, *8*, 19375.
[35] S. K. Wilke, D. C. Dunand, *Acta Mater.* **2019**, *162*, 90.
[36] S. K. Wilke, D. C. Dunand, *J. Power Sources* **2020**, *448*, 227463.
[37] F. Hassanli, *Study on the Oxidation/Reduction Behavior of 75 wt% Fe-(25-x) wt% Ni-x wt% Cu Foams Fabricated by Freeze Casting for Application in Energy Storage Unit of Solid-State Iron-Air Battery*, School of Engineering, Shiraz University, Shiraz, Iran **2023**.
[38] A. E. Jakus, S. L. Taylor, N. R. Geisendorfer, D. C. Dunand, R. N. Shah, *Adv. Funct. Mater.* **2015**, *25*, 6985.
[39] S. L. Taylor, A. E. Jakus, R. N. Shah, D. C. Dunand, *Met. Part. Inks Adv. Eng. Mater.* **2017**, *19*, 1600365.
[40] J. A. Lewis, *Adv. Funct. Mater.* **2006**, *16*, 2193.
[41] B. Y. Ahn, D. Shoji, C. J. Hansen, E. Hong, D. C. Dunand, J. A. Lewis, *Adv. Mater.* **2010**, *22*, 2251.
[42] R. D. Farahani, M. Dubé, D. Therriault, *Adv. Mater.* **2016**, *28*, 5794.
[43] J. A. Carpenter, N. Passaleva, M. Häring, G. Mikl, A. R. Studart, *Adv. Mater. Technol.* **2023**, *8*, 2200971.
[44] J. A. Carpenter, Z. Saraw, A. Schwegler, T. Magrini, G. Kuhn, A. Rafsanjani, A. R. Studart, *Adv. Mater.* **2023**, *35*, 2207181.
[45] C. Kenel, N. R. Geisendorfer, R. N. Shah, D. C. Dunand, *Addit. Manuf.* **2021**, *37*, 101637.
[46] J. J. Bowen, S. Mooraj, J. A. Goodman, S. Peng, D. P. Street, B. Roman-Manso, E. C. Davidson, K. L. Martin, L. M. Rueschhoff, S. N. Schiffres, W. Chen, J. A. Lewis, M. B. Dickerson, *Mater. Today* **2022**, *58*, 71.
[47] B. Román-Manso, J. Muth, L. J. Gibson, W. Ruettinger, J. A. Lewis, *ACS Appl. Mater. Interfaces* **2021**, *13*, 8976.
[48] D. Erb, *Zenodo* **2022**.
[49] S. Pennell, D. Dunand, *Acta Mater.* **2022**, 118543.
[50] G.-D. Sun, G.-H. Zhang, X.-P. Ji, J.-K. Liu, H. Zhang, K.-C. Chou, *Int. J. Refract. Metals Hard Mater.* **2019**, *80*, 11.
[51] R. M. Estrella, *Hydrogen Reduction Route towards the Production of Nano-Grained Alloys.-Synthesis and Characterization of Fe 2 Mo Powder*.